# CHAPTER-4

## Z-Scheme $CsPbBr_3$/BiOBr heterojunction for selective semidehydrogenation of 1,2,3,4-tetrahydroisoquinoline to 3,4-dihydroisoquinoline

## 4.1. Introduction

Building on the success of Ni and Co cocatalysts in water-free C–N coupling via $H_2O_2$ production, this chapter introduces a Z-scheme heterojunction photocatalyst for 1,2,3,4-tetrahydroisoquinoline (THIQ) semidehydrogenation, enabling selective $H_2O_2$ generation while avoiding the formation of water, crucial for the stability of $CsPbBr_3$ QDs. The 3,4-dihydroisoquinoline (DHIQ) is a valuable intermediate in the drug, pharmaceutical, petrochemical, and agrochemical industries, and it can be synthesized by the semidehydrogenation of THIQ.

Semiconductor heterostructures offer tunable bandgap, strong optical properties, and enhanced optoelectronic performance for LEDs, solar cells, photocatalysis, and photoredox reactions.[1-3] Heterojunctions improve charge separation by combining component benefits.[4] Z-scheme heterojunctions, with oxidation and reduction photocatalysts, further enhance performance by (i) suppressing recombination, (ii) retaining active charge carriers, (iii) boosting light absorption, and (iv) extending carrier lifetimes.[5]

In this study, we constructed a Z-scheme heterojunction using BiOBr nanosheets (NSs) and $CsPbBr_3$ QDs for the semidehydrogenation of THIQ with triplet oxygen ($^3O_2$) as a green electron acceptor (**Figure 4.1**). BiOBr has gained attention for its visible-light photocatalytic activity, attributed to its layered structure, which promotes charge separation.[6] Its valence band is sufficiently positive to convert $O_2^{\bullet-}$ to singlet oxygen ($^1O_2$). However, BiOBr alone showed poor activity for activation of $^3O_2$ to $O_2^{\bullet-}$ under light.[7]

On the other hand, $CsPbBr_3$ has a sufficiently negative conduction band minimum (CBM) for single-electron reduction of $^3O_2$ to $O_2^{\bullet-}$.[8-10] Thus, the $CsPbBr_3$/BiOBr Z-scheme heterojunction enables activation of $^3O_2$ from air to $O_2^{\bullet-}$ and subsequently $^1O_2$, facilitating

organic transformations. $CsPbBr_3$ also offers excellent optoelectronic properties, including strong light absorption, high extinction coefficient, and superior charge mobility.[11] Its soft crystal lattice tolerates lattice mismatch, promoting stable heterojunction formation with various semiconductors.[12]

In this study, we investigated the photocatalytic selective semidehydrogenation of THIQ to DHIQ using Z-scheme catalysts. DHIQ is a key intermediate in pharmaceuticals, typically produced via THIQ semidehydrogenation.[13] While electrocatalytic $2e^-$ oxidation of THIQ using transition metal catalysts has been explored,[14,15] photocatalytic methods remain largely underdeveloped. The challenge lies in precisely controlling $2e^-/2H^+$ transfers to avoid full dehydrogenation, which favors aromatization to isoquinoline (IQ) (**Figure 4.1**).[16-18]

Recently, Wang group reported photocatalytic dehydrogenation of THIQ using h-BCN photocatalyst, but the process resulted in IQ formation.[19] Furthermore, Bahnemann group, using $Rh/TiO_2$ photocatalyst, produced a mixture of DHIQ and IQ.[17] These studies highlight that the semidehydrogenation of THIQ to DHIQ remains a highly challenging process. However, Shi group successfully utilized $Zn_3In_2S_6$ for the photocatalytic semidehydrogenation of THIQ using molecular $^3O_2$ as the electron acceptor.[20] In further advancement, Li group demonstrated semidehydrogenation of THIQ using $MoS_2/ZnIn_2S_4$ heterojunction.[21]

Building on the success of previous studies, we designed Z-scheme heterojunctions of x%-$CsPbBr_3$/BiOBr (Z-x, x = 10, 20, and 30 wt%) for controlled semidehydrogenation of THIQ, using $^3O_2$ as a green electron acceptor. The Z-scheme heterojunction optimizes band positions to generate $O_2^{\bullet-}$ and $^1O_2$ via $^3O_2$ activation, aiding the hydrogen abstraction process.[22] While $CsPbBr_3$ can produce $O_2^{\bullet-}$, it showed minimal DHIQ formation. In contrast, BiOBr yielded a moderate DHIQ (56%), while Z-20 achieved a high yield of 97%. The generation of $^1O_2$ proved

essential for selective semidehydrogenation to DHIQ.

The construction of Z-scheme heterojunctions was confirmed by spectroscopy. EIS, photocurrent, and PL studies showed improved charge separation and reduced recombination. Femtosecond transient absorption spectroscopy (fs-TAS) revealed faster exciton relaxation in Z-20 due to rapid carrier trapping.

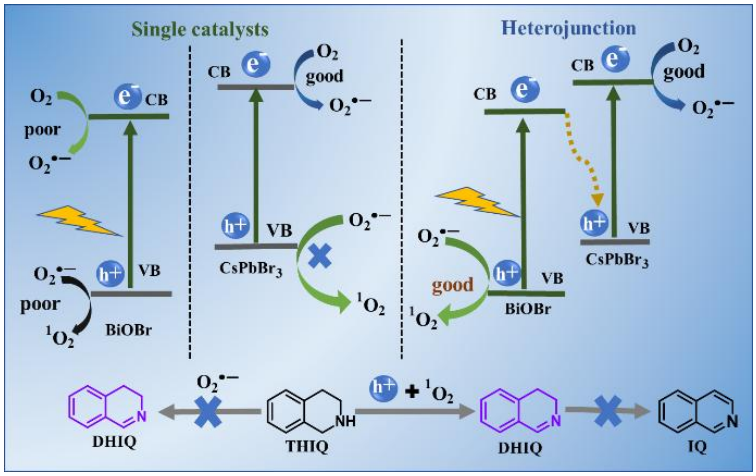


**Figure 4.1**. Schematic representation of molecular oxygen activation and hole utilization with $CsPbBr_3$/BiOBr heterojunction photocatalyst (Z-20) for the semidehydrogenation of 1,2,3,4-tetrahydroisoquinoline.

## 4.2. Chemicals

All the chemical details were mentioned in Chapter 2, Section 2.2.

## 4.3. Instruments

The same instruments described in Chapter 2, Section 2.3, were used for the spectroscopic, microscopic, and NMR characterization of the catalysts and products.

## 4.4. Experimental

### 4.4.1. Synthesis of $CsPbBr_3$ QDs

The $CsPbBr_3$ QDs methods described in Chapter 2, Section 2.3, were followed.

### 4.4.2. Synthesis of ultrathin BiOBr

Ultrathin BiOBr was synthesized using a previously reported solvothermal method. 1 mmol of KBr was added to 15 mL of ethanol and sonicated in an ultrasonic cleaner for 15 minutes. 1 mmol $Bi(NO_3)_3 \cdot 5H_2O$ was dissolved in 10 mL distilled water under stirring conditions for 10 minutes. Next, $Bi(NO_3)_3 \cdot 5H_2O$ solution was added to the KBr solution and continued stirring for 20 minutes. The mixture was then transferred to a 50 mL Teflon-lined stainless-steel autoclave and heated at 150 °C for 4 hours. The resulting precipitates were washed with ethanol and deionized water, then dried at 60 °C overnight.

### 4.4.3. Construction of heterojunction (Z-20)

In a typical process, 10 mL of $CsPbBr_3$ colloidal solution (Toluene: 1 mg/mL) was mixed with an appropriate amount of BiOBr. The mixture was ultrasonicated for 15 minutes and stirred in the dark for 2 hours. It was then centrifuged at 12000 rpm for 5 minutes, washed with hexane, and vacuum dried at 60 °C for 12 hours. The different wt.% of $CsPbBr_3$ in the $CsPbBr_3$/BiOBr heterojunction is mentioned in Table S1.

**Note:** CdS,[23] $WO_3$,[24] and $TiO_2$[25] were synthesized following previously reported methods. Further, the heterojunctions ($CsPbBr_3/WO_3$, CdS/BiOBr, and $TiO_2$/BiOBr) were constructed as shown in Table 4.1.

**Table 4.1**. Description of the photocatalysts.

| S.N. | Photocatalyst-I | Photocatalyst-II | Heterojunction photocatalyst |
|---|---|---|---|
| 1 | 10 mg $CsPbBr_3$ | 90 mg BiOBr | Z-10 |
| 2 | 20 mg $CsPbBr_3$ | 80 mg BiOBr | Z-20 |
| 3 | 30 mg $CsPbBr_3$ | 70 mg BiOBr | Z-30 |
| 4 | 20 mg $CsPbBr_3$ | 80 mg $WO_3$ | $CsPbBr_3/WO_3$ |
| 5 | 20 mg CdS | 80 mg BiOBr | CdS/BiOBr |
| 6 | 20 mg $TiO_2$ | 80 mg BiOBr | $TiO_2$/BiOBr |

## 4.5. Results and discussion

### 4.5.1. Syntheses and characterizations of heterojunction catalysts

BiOBr NSs were synthesized via a solvothermal method, and $CsPbBr_3$ by hot injection.[26,27] Z-10, Z-20, and Z-30 heterojunctions were made by physically mixing 10, 20, and 30 wt.% $CsPbBr_3$ with BiOBr (**Table 4.1**). While all Z-schemes enhanced charge transport and $^3O_2$

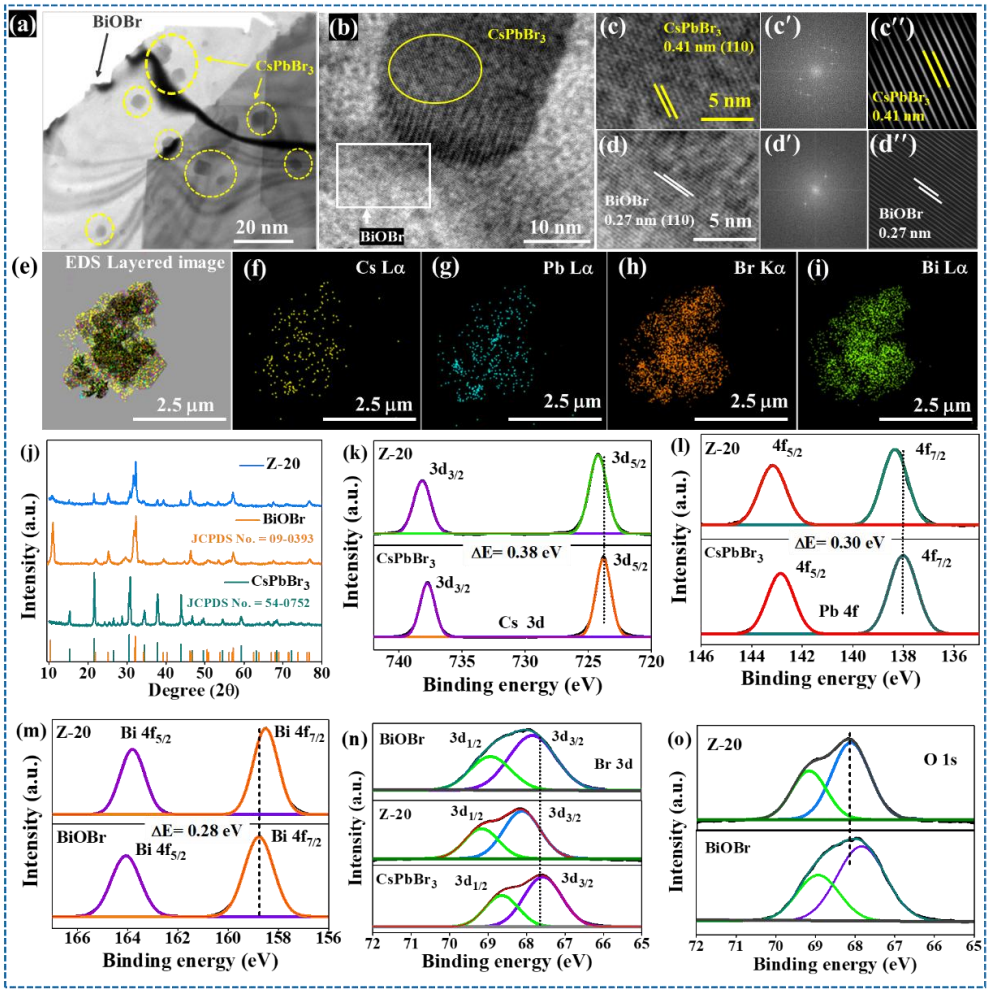


**Figure 4.2.** (a) TEM image of Z-20 showing the deposition of $CsPbBr_3$ QDs on the surface of BiOBr nanosheets. $CsPbBr_3$ QDs on the surface of BiOBr are marked with circles. (b) HR-TEM confirmed the formation of heterojunction of QDs and BiOBr. (c,d) The lattices are 0.41 nm for $CsPbBr_3$ QDs and 0.27 nm for BiOBr, corresponding to (110) planes of both semiconductors. (c′ and d′) Selected area FFT showing the diffractions for $CsPbBr_3$ and BiOBr in Z-20. (c″ and d″) are the Inverse FFT of figures c′ and d′, respectively. (e-i) EDX elemental mapping of Z-20. (j) PXRD patterns of $CsPbBr_3$, BiOBr, and Z-20. (k) Cs 3d XP spectra of $CsPbBr_3$, and Z-20; (l) Pb 4f XP spectra of $CsPbBr_3$, and Z-20; and (m) Bi 4f XP spectra of BiOBr, and Z-20. (n) Br 3d XPS of Z-20, $CsPbBr_3$, and BiOBr. (o) O 1s XPS of Z-20 and BiOBr.

activation compared to individual components, Z-20 (20% loading) showed the highest photoactivity (see later). Thus, detailed characterization was focused on Z-20 and compared with bare BiOBr and $CsPbBr_3$.

The transmission electron microscopy (TEM) analysis showed that $CsPbBr_3$ had an average size of 6 ± 2 nm (**Figure 4.2a**). HR-TEM confirmed heterojunction formation with BiOBr (**Figure 4.2b**), revealing lattice spacings of 0.27 nm for BiOBr (110) and 0.413 nm for $CsPbBr_3$ (110) (**Figure 4.2c-d**). FFT and inverse FFT analyses further validated these spacings (**Figure 4.2c′–d′, c″–d″**). EDX spectra confirmed the elemental composition of $CsPbBr_3$, BiOBr, and Z-20, while EDX mapping showed uniform elemental distribution in Z-20 (**Figure 4.2e–i**).

Powder X-ray diffraction (PXRD) of Z-20 showed characteristic peaks of both $CsPbBr_3$ (cubic, Pm-3m, JCPDS 54-0752) and BiOBr (tetragonal, P4/nm, JCPDS 73-2061) (**Figure 4.2j**).[12,27] A reduced (001) peak intensity in Z-20 suggests $CsPbBr_3$ QDs are deposited on the (001) facet of BiOBr NSs (**Figure 4.2j**). X-ray photoelectron spectroscopy (XPS) was used to probe electronic interactions between BiOBr and $CsPbBr_3$ in Z-20 (**Figure 4.2k-m**).[12,27] In Z-20, the binding energies of Cs 3d, Pb 4f, and Br 3d shifted positively compared to pristine $CsPbBr_3$, indicating an electron-deficient state in $CsPbBr_3$ after the integration with BiOBr (**Figure 4.2k, l, n**). On the other hand, Bi in Z-20 turns into more electron-rich (negative shift in the BEs of Bi 4f in Z-20) compared to that in BiOBr to balance the electron redistribution in Z-20 (**Figure 4.2m**). These shifts indicate electron transfer from $CsPbBr_3$ to BiOBr due to their band potential difference, generating an internal electric field (IEF) from $CsPbBr_3$ to BiOBr in the dark. The generation of the IEF facilitates the charge separation in Z-20 and improves the photocatalytic semidehydrogenation of THIQ. The O 1s XPS spectra of $CsPbBr_3$,

Z-20, and BiOBr are shown in **Figure 4.2o**.

### 4.5.2. Z-scheme *vs* type-II heterojunction

The ultraviolet-visible diffuse reflectance spectroscopy (UV-DRS) studies were carried out to understand the light absorption properties of $CsPbBr_3$, BiOBr, and Z-scheme photocatalysts (Z-10, Z-20, Z-30) (**Figure 4.3a**).[12,27] $CsPbBr_3$ and BiOBr showed absorption peaks at 518 nm and 440 nm, respectively. The heterojunction Z-20 exhibited absorption behaviour between that of $CsPbBr_3$ and BiOBr, indicating strong electronic interactions. The Tauc plot calculated the bandgaps as 2.32 eV for $CsPbBr_3$ and 2.77 eV for BiOBr NSs. Interestingly, the bandgap of $CsPbBr_3$ remained unchanged after being loaded on the surface of BiOBr, attributed to the strong absorption properties of $CsPbBr_3$ (**Figure 4.3a inset**).

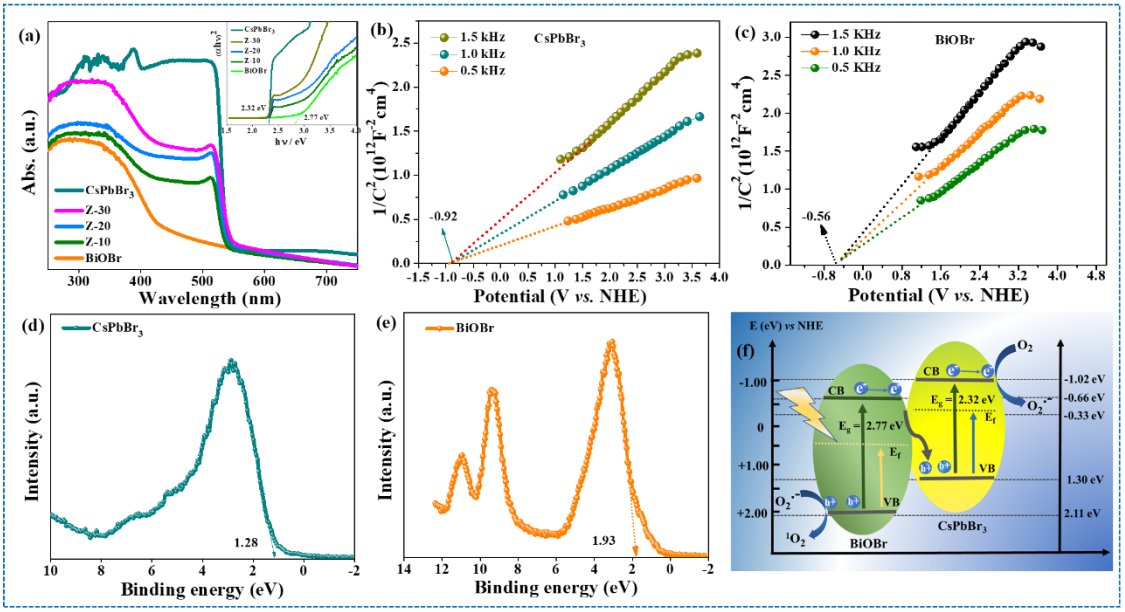


**Figure 4.3.** (a) The UV-vis. diffuse reflectance spectra of $CsPbBr_3$ QDs, Z-20, and BiOBr, inset showing Tauc plot corresponding to figure (a), no significant change in the bandgap of $CsPbBr_3$ after the introduction of the $CsPbBr_3$ QDs to BiOBr nanosheets. (b, c) Mott-Schottky plots of $CsPbBr_3$ and BiOBr. (d, e) Valence band XPS of (d) $CsPbBr_3$ and (e) BiOBr. (f) Depiction of the conduction band minima and valence band maxima for $CsPbBr_3$ QDs and BiOBr NSs, derived from Tauc plot and Mott–Schottky studies.

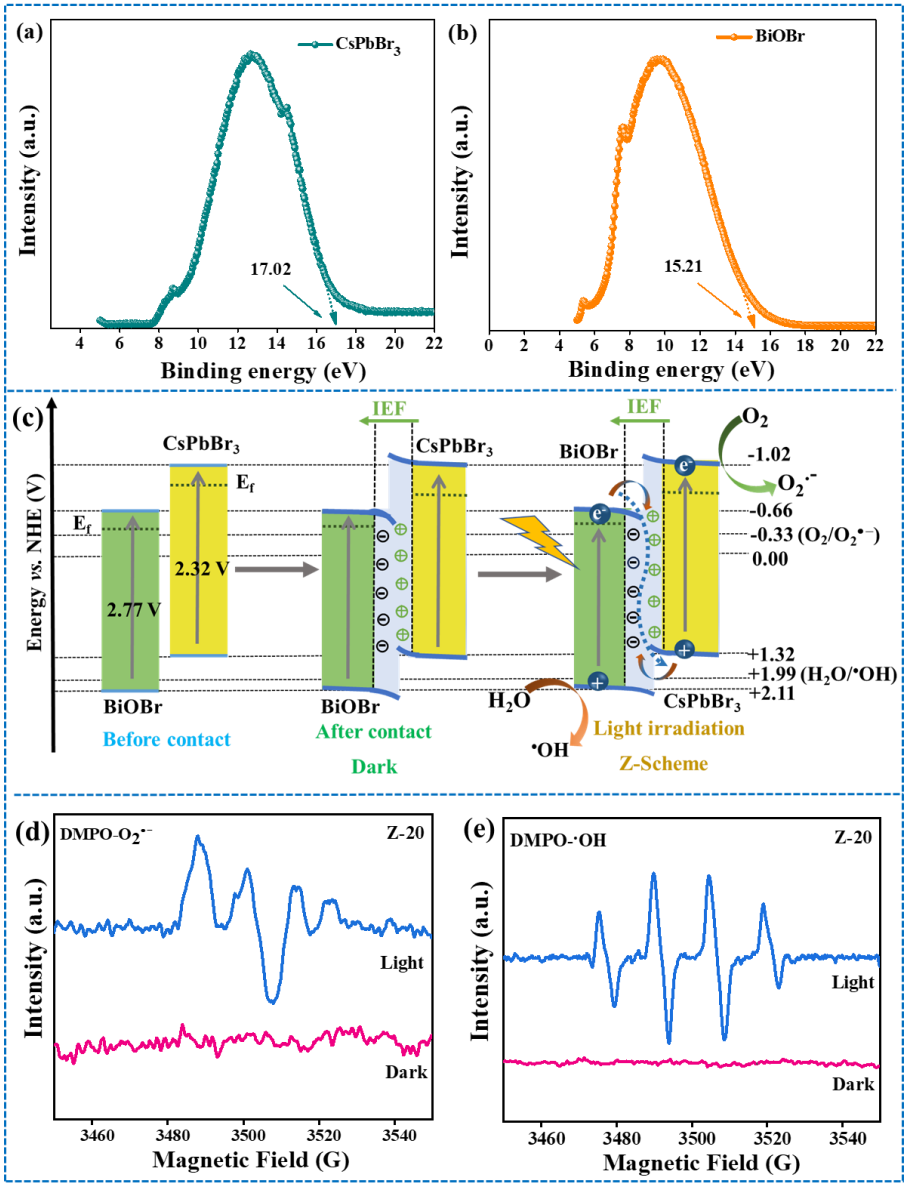


**Figure 4.4.** (a and b) UPS spectra showing the secondary electron cut-off for $CsPbBr_3$ and BiOBr photocatalysts were analyzed. The end energy levels (EEL) of $CsPbBr_3$ and BiOBr were measured as 17.02 eV and 15.21 eV, respectively. Using the Fermi level ($E_F$) and the equation $\Phi = 21.2 - EEL$, the work functions ($\Phi$) of $CsPbBr_3$ and BiOBr were calculated to be 4.2 eV and 6.01 eV, respectively. (c) Schematic representation of BiOBr/$CsPbBr_3$ heterojunction: internal electric field (IEF) induced charge transfer, separation, and the formation of Z-scheme heterojunction under UV–Visible light irradiation for photocatalytic semidehydrogenation of THIQ. (d) ESR spectra of DMPO-$O_2^{\bullet-}$ and (e) DMPO-$^{\bullet}$OH.

Mott-Schottky (MS) analysis confirmed the formation of an n–n heterojunction between $CsPbBr_3$ and BiOBr (**Figure 4.3b-c**). The flat band potentials ($E_{fb}$) were −0.92 eV vs. NHE for

$CsPbBr_3$ and −0.56 eV vs. NHE for BiOBr. Correspondingly, the conduction band edges ($E_{CB}$) were −1.02 eV for $CsPbBr_3$ and −0.66 eV for BiOBr. Based on these, the valence band maxima ($E_{VB}$) were calculated as 1.32 eV and 2.11 eV vs. NHE for $CsPbBr_3$ and BiOBr, respectively.

Furthermore, valence band XPS analysis was performed to determine the energy difference between the valence band maximum (VBM) and Fermi level ($E_F$) of the catalysts.[2,3] The $E_F$−$E_{VB}$ values were 1.28 eV for $CsPbBr_3$ and 1.93 eV for BiOBr (**Figure 4.3d-e**). These values were used to construct the band alignment diagram for $CsPbBr_3$, BiOBr, and Z-20 (**Figure 4.3f**). The staggered band alignment supports Z-scheme/type-II heterojunction formation (**Figure 4.4**). With BiOBr's $E_F$ lower than $CsPbBr_3$'s, Z-scheme formation is favorable under light. Under visible light irradiation, electrons transfer from the CB of BiOBr to the VB of $CsPbBr_3$, promoting efficient charge separation. Additional evidence for this Z-scheme mechanism is provided in the next section.

### 4.5.3. Z-Scheme heterojunction

The work function (Φ) values determined by ultraviolet photoelectron spectroscopy (UPS), 4.20 eV for $CsPbBr_3$ and 6.01 eV for BiOBr, confirm a surface potential flow from BiOBr to $CsPbBr_3$ in the Z-20 composite (**Figure 4.4 a-b**). The higher work function of BiOBr indicates a lower Fermi level ($E_F$) compared to $CsPbBr_3$.[28-30] As a result, when the two materials are in close contact (in the dark), electrons spontaneously transfer from $CsPbBr_3$ to BiOBr until their Fermi levels align. This charge redistribution forms an electron depletion layer in $CsPbBr_3$ and an accumulation layer in BiOBr. Consequently, $CsPbBr_3$ becomes positively charged while BiOBr becomes negatively charged at the interface, creating band bending and a built-in electric field pointing from $CsPbBr_3$ to BiOBr (**Figure 4.4c**). This interfacial field facilitates photoinduced electron transfer from the CB of BiOBr to recombine with photoinduced holes

in the VB of $CsPbBr_3$, characteristic of a Z-scheme mechanism. This Z-scheme structure enhances charge carrier separation, preserving electrons in the CB of $CsPbBr_3$ and holes in the VB of BiOBr for improved photocatalytic activity (**Figure 4.4c**).

To further investigate the charge transfer mechanism in Z-20, electron spin resonance (ESR) analysis was performed. The spin-trapping agent 5,5-dimethyl-1-pyrroline N-oxide (DMPO) was used to detect photogenerated reactive oxygen species, particularly $O_2^{\bullet-}$ (**Figure 4.4d-e**).[2] Under simulated sunlight, Z-20 exhibited distinct DMPO-$O_2^{\bullet-}$ signals with four characteristic peaks in a 1:1:1:1 intensity ratio, while no signals were detected under dark conditions (**Figure 4.4d**).[3] This indicates that photoexcitation is required for $O_2^{\bullet-}$ generation. Given that the conduction band edge ($E_{CB}$) of Z-20 is sufficiently negative to reduce $O_2$, the strong DMPO-$O_2^{\bullet-}$ signals suggest efficient accumulation of photoexcited electrons in the conduction band of $CsPbBr_3$ (**Figure 4.4d**).

To confirm the formation of Z-scheme and not type-II heterojunction, we have introduced $H_2O$ in the reaction mixture. The $^{\bullet}OH$ radicals formation confirms the Z-scheme heterojunction formation between $CsPbBr_3$ and BiOBr. The type-II heterojunction cannot produce $^{\bullet}OH$ radicals because of the low VBM. In the EPR spectroscopy, Z-20 showed four characteristic peaks (1:2:2:1) of DMPO-$^{\bullet}OH$ adducts (**Figure 4.4e**).[2] These findings strongly support that the charge transfer in the Z-20 system follows a Z-scheme mechanism rather than a type-II process.

### 4.6. Charge transfer dynamics

Photocurrent measurements were conducted to evaluate the separation efficiency of photogenerated electron–hole pairs (**Figure 4.5a**). Generally, a higher photocurrent density reflects more effective charge separation.[31] Both BiOBr and $CsPbBr_3$ showed relatively low

photocurrent densities, indicating inefficient separation of photoinduced carriers. In contrast, the heterojunction significantly improved the photocurrent response, with Z-20 displaying the highest photocurrent among all samples, including Z-10 and Z-30 (**Figure 4.5a**). This result confirms that Z-20 exhibits superior charge carrier separation efficiency. Electrochemical impedance spectroscopy (EIS) showed the charge transport properties of the photocatalysts. Z-20 showed the lowest charge transfer resistance than $CsPbBr_3$ and BiOBr (**Figure 4.5b**).

The strong photoluminescence (PL) emissions were observed for bare BiOBr and $CsPbBr_3$ at 483 nm and 520 nm, respectively. Upon formation of the Z-scheme heterojunction, the PL intensity decreased in the order: Z-30 > Z-10 > Z-20 (**Figure 4.5c**). This reduction in PL intensity reflects suppressed radiative recombination of photogenerated charge carriers, indicating improved charge separation. Notably, the PL of BiOBr was quenched across all compositions, regardless of the $CsPbBr_3$ loading (**Figure 4.5c**), further supporting efficient interfacial charge transfer in the Z-scheme system.

**4.7. Femtosecond transient absorption spectroscopy study**

The fs-TAS study was conducted to understand the ultrafast exciton recombination dynamics in bare $CsPbBr_3$ QDs and Z-20 heterostructure. The $CsPbBr_3$ QDs were excited at 370 nm, above their band edge, to generate charge carriers and induce trap state formation.[32] The TA spectra of $CsPbBr_3$ revealed two distinct features: (i) a strong photo-induced absorption (PIA) in the blue region (450–515 nm, peaking at 505 nm), attributed to probe-induced excitation of photoexcited carriers, and (ii) a broad photo-induced bleach (PIB) in the red region (520–600 nm, with a maximum at 518 nm), associated with ground-state bleaching and stimulated emission (**Figures 4.5d and 4.6a**).[33]

Similarly, the Z-20 heterostructure, also excited at 370 nm, exhibited TA spectra shown

in **Figures 4.5e and 4.6b**. In this case, the PIA and PIB bands were centred at 511 nm and 525 nm, respectively. The PIB signal, related to ground-state bleaching due to electron state filling, was reduced in the Z-20 sample, indicating altered carrier dynamics upon heterostructure formation.

We analyzed the kinetic traces at various probe wavelengths to monitor the evolution and relaxation of trap states (**Figure 4.5f–i**). These kinetics were fitted using a sum of exponential functions, including a long-lived component, with the extracted parameters summarized in **Table 4.2**. The spectral evolution dynamics differed markedly between the $CsPbBr_3$ QDs and the Z-20 heterostructure. Kinetic traces at 490 nm and 500 nm correspond to the PIA region (**Figures 4.5f and 4.5g**), while the trace at 550 nm reflects the recovery of ground-state bleach from a higher energy state. Additionally, features of the PIB band align well with the UV absorption bands (**Figures 4.5h and 4.3a**).

The decay traces indicate that photogenerated electron relaxation follows a three-step pathway. The deposition of $CsPbBr_3$ onto BiOBr significantly accelerates the relaxation kinetics, as evidenced by the TA measurements. At 500 nm, both $CsPbBr_3$ QDs and the Z-20 heterostructure show an initial rise in the PIA signal; however, the decay occurs much more rapidly in Z-20 (**Figure 4.5h**). The extracted lifetimes at 500 nm are 100 ± 20 ps and 1300 ± 200 ps for $CsPbBr_3$, and 20 ± 2 ps and 700 ± 200 ps for Z-20 (**Table 4.2**).[34] Notably, the 100 ± 20 ps component in $CsPbBr_3$, associated with excited electron decay, shortens by nearly an order of magnitude to 20 ± 2 ps in Z-20, highlighting more efficient charge transfer or trapping processes in the heterostructure.

In $CsPbBr_3$, the recovery of the bleach at 550 nm was fitted to 60 ± 10 ps and 750 ± 100 ps, which were reduced to 17 ± 0.2 ps and 200 ± 22 ps in Z-20. Similar trends were observed

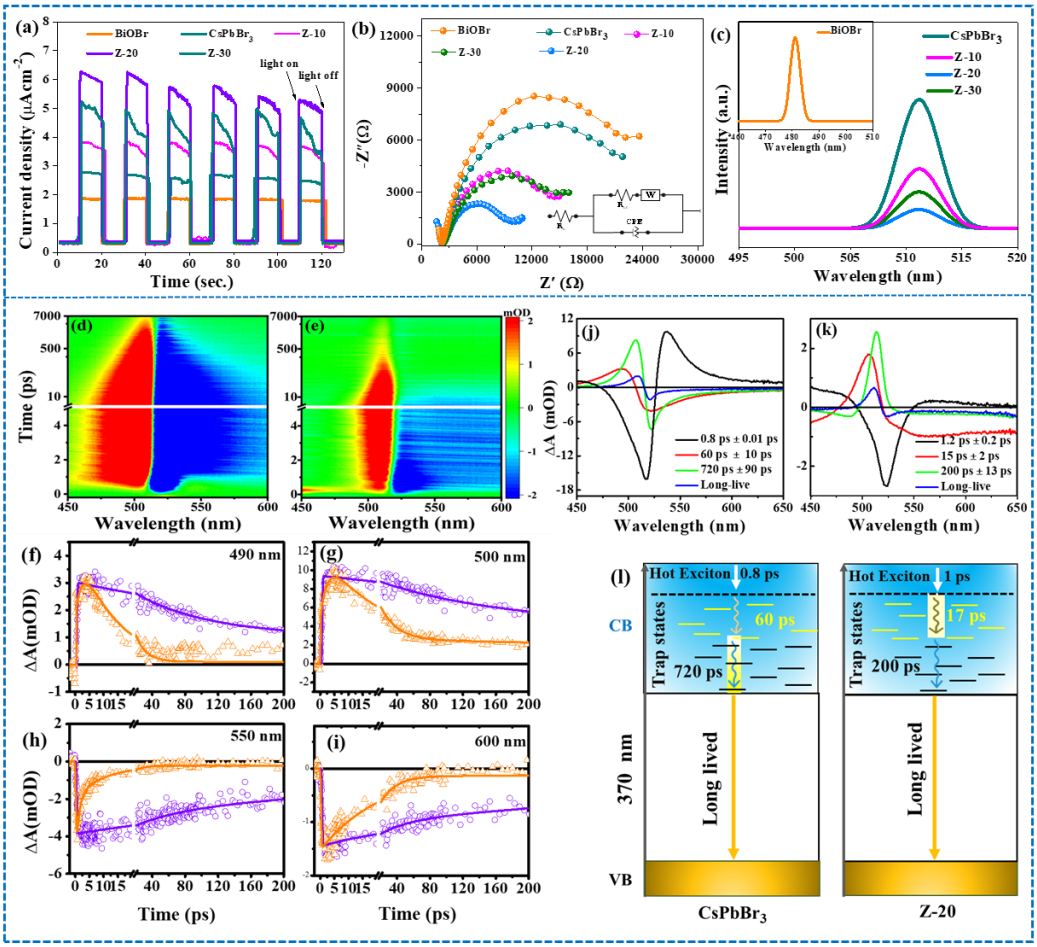


**Figure 4.5.** (a) Photocurrent of BiOBr, $CsPbBr_3$, and heterojunction Z-20 under light/dark conditions. (b) EIS of BiOBr, $CsPbBr_3$ and Z-20. (c) PL spectra of $CsPbBr_3$ and Z-20 at 370 nm excitation wavelength (Inset image shows the PL spectra of BiOBr at 335 nm excitation wavelength). (d) TA spectra of $CsPbBr_3$, (e) TA spectra of Z-20. Kinetic traces for $CsPbBr_3$ (violet) and Z-20 (orange) at probe wavelength (f) 490 nm (g) 500 nm (h) 550 nm and (i) 600 nm, the solid lines are fitted lines. (j, k) the decay-associated spectra (DAS) of $CsPbBr_3$ and Z-20. (l) A schematic depiction of the formation and relaxation of charge carriers in $CsPbBr_3$ and Z-20.

for other wavelengths as well (**Figure 4.5i and Table 4.2**).[35] The evolution-associated difference spectra (EADS)[36] identified three ultrafast components in $CsPbBr_3$ QDs and Z-20 (**Figure 4.5j-k**). The global analysis revealed lifetimes are 0.8 ± 0.01 ps, 60 ± 10 ps, and 720 ± 90 ps for $CsPbBr_3$ (**Figure 4.5j**) and 1.2 ± 0.2 ps, 15 ± 2 ps, and 200 ± 13 ps for Z-20 (**Figure 4.5k**). Additionally, a long-lived component associated with the charge recombination process

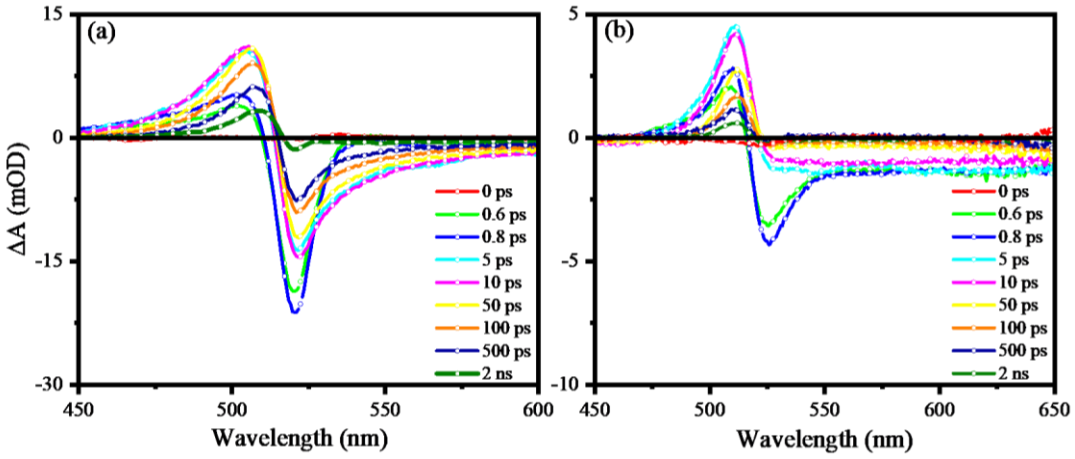


**Figure 4.6.** The transient absorption (TA) spectra at different delay times between pump and probe (a) $CsPbBr_3$, (b) Z-20.

**Table 4.2.** Fitting coefficient of kinetics traces at 490 nm, 500 nm, 550 nm, and 600 nm of $CsPbBr_3$ and Z-20 excited at 370 nm.

| Compound | Wavelength (nm) | $\tau_1$ (ps) ($a_1$) | $\tau_2$ (ps) ($a_2$) | $\tau_3$ (ps) ($a_3$) |
|---|---|---|---|---|
| $CsPbBr_3$ | 490 | 76 ± 10<br>0.0031 ±0.0004 | 800 ± 250<br>0.0022 ±0.0004 | Long Lived |
| | 500 | 100 ± 20<br>0.0040 ±0.0003 | 1300 ± 200<br>0.0044 ±0.0003 | Long Lived |
| | 550 | 60 ± 10<br>-0.0024 ±0.0005 | 750 ± 100<br>-0.0052 ±0.0005 | Long Lived |
| | 600 | 32 ± 3<br>-0.00056 ±0.00001 | 400 ± 70<br>0.0044 ±0.0003 | Long Lived |
| Z-20 | 490 | 3 ± 1<br>0.0013 ±0.0004 | 12 ± 4<br>-0.0007 ±0.0003 | Long Lived |
| | 500 | 20 ± 1<br>0.0019 ±0.0001 | 700 ± 100<br>0.0044 ±0.0003 | Long Lived |
| | 550 | 17 ± 0.2<br>-0.0014 ±0.0003 | 200 ± 22<br>-0.0023 ±0.0001 | Long Lived |
| | 600 | 0.4 ± 0.1<br>-0.0029 ±0.0003 | 13 ±2.2<br>-0.0013 ±0.0001 | Long Lived |

was also observed. This is consistent with a nondecaying signal in the TA measurements.

Previous time-resolved photoluminescence studies have reported recombination lifetimes of approximately 10 ns for $CsPbBr_3$.[3,37] The significantly faster decay observed in the Z-20 heterostructure is attributed to an enhanced depopulation of excited states, suggesting the

presence of additional trap states in $CsPbBr_3$ upon heterojunction formation. Similar behavior has been noted in $CsPbBr_3$, benzoquinone systems, where trap state dynamics on the nanosecond to picosecond scale contributed to improved catalytic performance.[38,39] In this study, TA measurements were used to determine the lifetimes associated with exciton formation and relaxation in both $CsPbBr_3$ and Z-20 (**Figure 4.5l**). These lifetimes were further used to calculate rate constants for the ultrafast processes. A marked reduction in the trap-state formation time, from 60 ± 10 ps in $CsPbBr_3$ to 17 ± 0.2 ps in Z-20, was observed. This corresponds to a calculated trap-state formation rate constant of $k_{trap} = 4.2 \times 10^{10}\ s^{-1}$.

The observed hot electron transfer rate aligns well with values reported in previous studies on similar nanostructures.[40-43] The faster trap-state formation in Z-20, compared to pristine $CsPbBr_3$ QDs, is attributed to efficient hot electron transfer within the heterojunction. These photogenerated electrons leave behind holes in the VB of BiOBr, which then interact with THIQ to generate the iminium radical cation. Simultaneously, hot electrons in the CB of $CsPbBr_3$ $^3O_2$ produce $O_2^{\bullet-}$, thereby initiating the dehydrogenation reaction.

### 4.8. Photocatalytic semidehydrogenation reaction

The photoredox semidehydrogenation of THIQ was tested in various solvents, with acetonitrile showing the highest activity (**Table 4.3**). The control experiments confirmed the necessity of light, $O_2$, and the photocatalyst. $CsPbBr_3$ QDs showed minimal activity, BiOBr gave 56% DHIQ yield, while the Z-20 heterojunction achieved complete conversion with 97% selectivity (**Figure 4.7a**).

It is important to note that the interaction between substrate molecules and the microstructure of the catalyst surface has been addressed in previous studies. Aromatic molecules, such as those containing phenyl rings, typically adsorb onto specific Lewis's acid

**Table 4.3**. Photocatalytic optimization conditions of semi-dehydrogenation of 1,2,3,4-Tetrahydroisoquinoline.

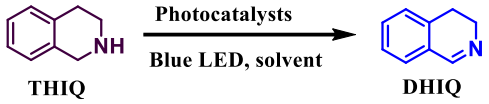


THIQ DHIQ

| S.N. | Photocatalyst | Solvent | Conditions | Light/Dark | Time (h) | % Conversion of THIQ (1) | % Isolated Yield of DHIQ (2) |
|---|---|---|---|---|---|---|---|
| **Variation of catalysts** | | | | | | | |
| 1 | $CsPbBr_3$ | $CH_3CN$ | Air | Blue LED | 6 | Trace | Trace |
| 2 | BiOBr | $CH_3CN$ | Air | Blue LED | 6 | 57 | 56 |
| 3 | Z-10 | $CH_3CN$ | Air | Blue LED | 6 | 78 | 76 |
| **4** | **Z-20** | **$CH_3CN$** | **Air** | **Blue LED** | **6** | **99** | **97** |
| 5 | Z-30 | $CH_3CN$ | Air | Blue LED | 6 | 83 | 80 |
| **Variation of solvents** | | | | | | | |
| 6 | Z-20 | THF | Air | Blue LED | 6 | 69 | 64 |
| 7 | Z-20 | MeOH | Air | Blue LED | 6 | 85 | 77 |
| 8 | Z-20 | EtOH | Air | Blue LED | 6 | 89 | 81 |
| **9** | **Z-20** | **$CH_3CN$** | **Air** | **Blue LED** | **6** | **99** | **97** |
| 10 | Z-20 | 1,4-Dioxane | Air | Blue LED | 6 | 75 | 74 |
| 11 | Z-20 | Toluene | Air | Blue LED | 6 | 58 | 53 |
| 12 | Z-20 | DMF | Air | Blue LED | 6 | 33 | 28 |
| **Other variations in the reaction conditions** | | | | | | | |
| 13 | - | $CH_3CN$ | Air | Blue LED | 6 | No reaction | No reaction |
| 14 | Z-20 | $CH_3CN$ | Air | Dark | 6 | ~ 4 | ~ 4 |
| 15 | Z-20 | $CH_3CN$ | Pure $O_2$ | Blue LED | 3 | 99 | 97 |

**Reaction conditions:** 10 mg catalyst, 0.5 mmol 1,2,3,4-tetrahydroisoquinoline, and 3 mL solvent were mixed and irradiated with a 15 W blue LED, maintaining a temperature of 34 ± 4 °C for the mentioned time.

sites on the catalyst surface.[44] On BiOBr, $Bi^{3+}$ ions act as Lewis acid sites, facilitating such interactions between the substrate and the catalyst surface.[7,44]

The time-monitored conversion data with Z-20 showed that the full conversion of THIQ was achieved after 6 hours (**Figure 4.7b**). Interestingly, the extension of the reaction time to 10 hours did not lead to the further conversion of DHIQ into IQ (**Figure 4.7b**). The results confirm that the Z-20 heterojunction has a controlled oxidation band potential (VB) suitable

for the selective semidehydrogenation of THIQ to DHIQ.

Interestingly, while indoline undergoes a $2e^-$ oxidation to form indole, 1,2,3,4-tetrahydroquinoline (THQ) requires a $4e^-$ dehydrogenation to produce quinoline. The selective $2e^-$ oxidation of THIQ to DHIQ by Z-20 is therefore notable. In most prior photocatalytic studies, THIQ primarily followed a $4e^-$ pathway to form IQ, with only limited reports detecting DHIQ as an intermediate. Recent advances have achieved selective $2e^-$ oxidation using expensive In-based photocatalysts like $Zn_3In_2S_6$, $MoS_2/ZnIn_2S_4$, and $ZnIn_2S_4$. The Z-20 thus presents a cost-effective alternative for selective THIQ semidehydrogenation.

The selective oxidation of DHIQ to IQ ($2e^-$ process) was effectively suppressed by selecting photocatalysts with suitably positioned valence band maxima (VBM) in the heterojunction. Oxidizing DHIQ to IQ requires a VBM more positive than THIQ's oxidation potential (2.71 V vs. NHE). To investigate this, a $CsPbBr_3/WO_3$ heterojunction, featuring a more positive VBM (3.06 V vs. NHE)[20], was tested. As anticipated, it achieved 81% total conversion after 10 hours, yielding 24% DHIQ and 57% IQ (**Figure 4.7c**), confirming that a more positive VBM promotes full oxidation to IQ. Similarly, CdS/BiOBr and $TiO_2$/BiOBr systems gave 74% and 65% DHIQ yields, respectively. Their comparatively lower selectivity is attributed to inefficient $O_2$ activation to $O_2^{\bullet-}$. Overall, the $CsPbBr_3$/BiOBr (Z-20) system exhibited the highest activity and selectivity for the controlled $2e^-$ semidehydrogenation of THIQ to DHIQ.

### 4.9. Mechanistic study of semidehydrogenation

In the Z-20 system, photogenerated electrons in the CB of $CsPbBr_3$ activate adsorbed oxygen on the Pb sites, generating $O_2^{\bullet-}$, which are subsequently oxidized to $^1O_2$ via holes in the VB of BiOBr.[8-10] The THIQ molecule interacts with VB holes to form a cationic radical intermediate

(A) (**Figure 4.7d**).[20,21,43] The resulting $^1O_2$ abstracts a hydrogen atom from this cationic radical, yielding a secondary cationic intermediate (I*) and a hydroperoxyl radical (•OOH). Notably, intermediate I* was confirmed through the formation of a TEMPO adduct. Finally, the •OOH radical reacts with I* to produce the desired product, DHIQ, along with $H_2O_2$.

In addition to EPR studies, $O_2^{\bullet-}$ radicals were detected by *P*-Nitro-Blue tetrazolium chloride (NBT) test via UV-visible absorption spectroscopy (**Figure 4.7e**).[46,47] The NBT test confirmed that the Z-20 showed a higher amount of $O_2^{\bullet-}$ formation by molecular oxygen activation compared to single catalysts ($CsPbBr_3$ or BiOBr) (**Figure 4.7e**). Furthermore, EPR spin-trapping experiments were conducted using TEMP as the trapping agent, confirming the $^1O_2$ formation in the reaction (**Figure 4.7f**).

Additionally, 9,10-diphenylanthracene (DPA) was employed as a probe to detect $^1O_2$, characterized by its distinct UV–vis absorption peaks at 337, 355, 373, and 395 nm (**Figure 4.8a**). Upon generation of $^1O_2$, DPA undergoes oxidation, resulting in a decrease in its absorption signals. The rate of signal quenching directly correlates with the rate of $^1O_2$ production. A gradual decline in DPA absorption intensity under light irradiation confirms that Z-20 effectively generates $^1O_2$ under photocatalytic conditions. Moreover, $^1O_2$ was found to actively participate in the semidehydrogenation of THIQ by working synergistically with photogenerated holes ($h^+$). In this mechanism, $h^+$ facilitates the oxidation of THIQ, producing a hydrogen atom and a reactive iminium radical cation, while $^1O_2$ abstracts $H^+$ to produce hydroperoxide radical (•OOH) and cationic intermediate ($I^{\#}$). The singlet oxygen $^1O_2$ can be generated via two primary pathways: (i) energy transfer from $^3O_2$, and (ii) electron transfer from $O_2^{\bullet-}$.[20,48] In semiconductor systems, it is well established that $O_2^{\bullet-}$ can be oxidized by photogenerated $h^+$ to form $^1O_2$ via the reaction $O_2^{\bullet-} + h^+ \rightarrow {}^1O_2$. The formation of $H_2O_2$

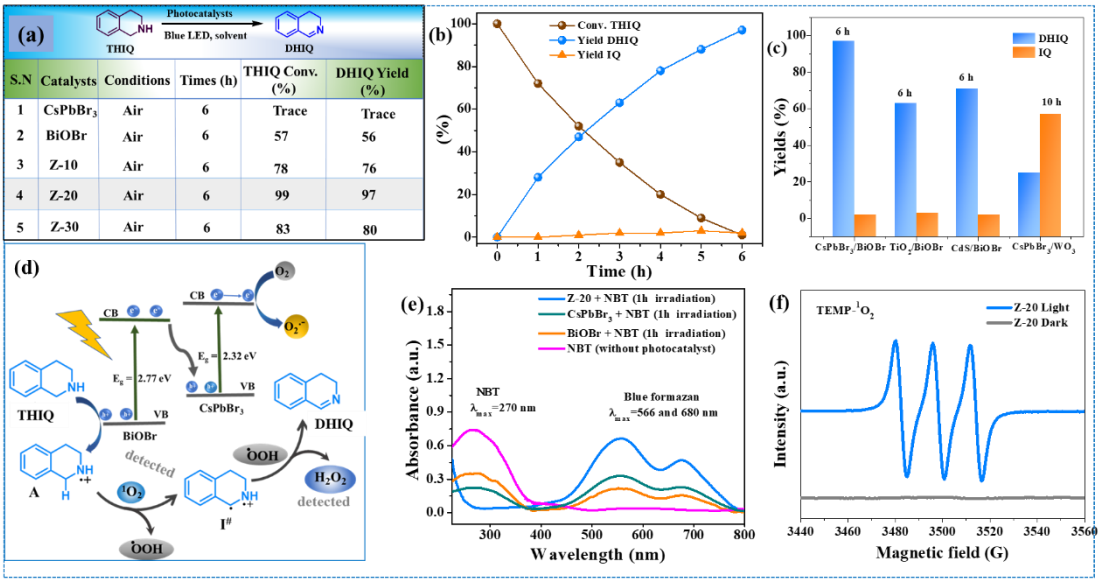


**Figure 4.7**. (a) Photocatalytic test with all catalysts. (b) Time-dependent conversion of 1,2,3,4-tetrahydroisoquinoline and DHIQ products formed with Z-20 heterojunction in air and light. After achieving the highest yield of DHIQ not convert into IQ with increasing reaction time. (c) Different heterostructure photocatalysts for semidehydrogenation of THIQ in air. (d) Proposed mechanism of semidehydrogenation of THIQ. (e) Detection of photogenerated superoxide radicals (NBT test). (f) $^1O_2$ radical trapping by EPR spectroscopy.

**Reaction conditions:** 10 mg catalyst, 0.5 mmol THIQ, and 3 mL solvent were taken in a borosilicate reaction vial and irradiated with a 15 W blue LED at temperature of 34 ± 2°C for 6 hours. The product was isolated by column chromatography on a silica column using varying ratios of ethyl acetate and hexane as the eluent. The product's isolated yield was reported in all cases.

confirms this pathway. We performed a control experiment using a hole scavenger (triethylamine, TEA) in a system containing DPA and Z-20 (**Figure 4.8b**).[20,49] The presence of TEA significantly reduced the generation of $^1O_2$, as indicated by the diminished decrease in DPA absorption intensity compared to the reaction without the scavenger (**Figure 4.8b**). This supports the role of photogenerated holes in converting $O_2^{\bullet-}$ to $^1O_2$ in the Z-20 system.

Similarly, the photocatalytic production of $H_2O_2$ was detected using the o-tolidine test via UV–Visible absorption spectroscopy (**Figure 4.8bc**). The formation of $H_2O_2$ and the conversion of THIQ are closely linked to efficient charge separation and the reduction of

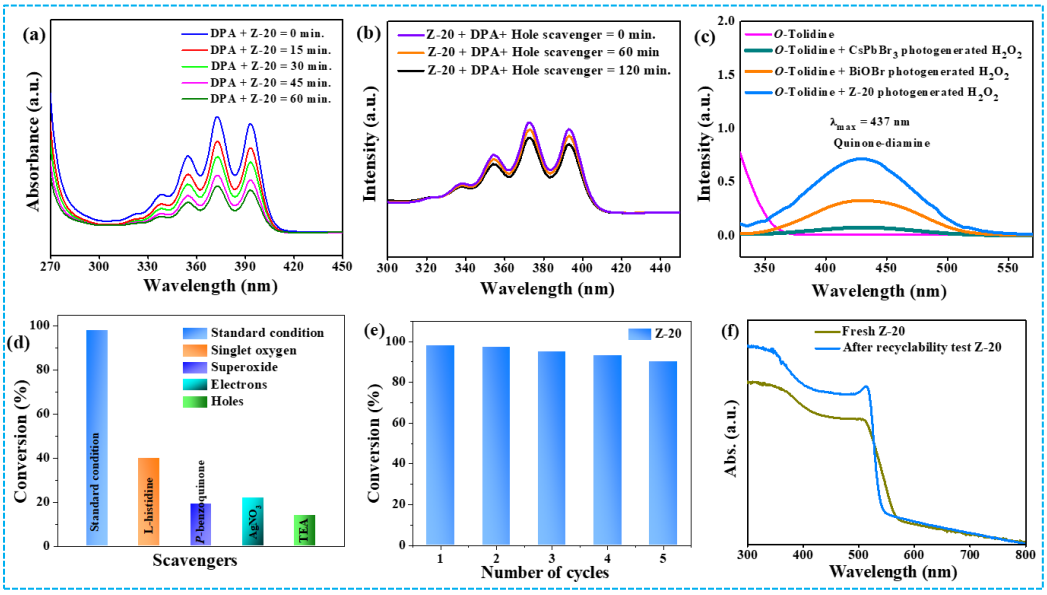


**Figure 4.8**. (a) UV-visible spectroscopy detects the photogenerated $^1O_2$. (b) $^1O_2$ generation through the reaction ($O_2^{\bullet-} + h^+ \rightarrow {}^1O_2$) process. (c) UV-visible spectroscopy detects the photogenerated $H_2O_2$ in the reaction mixture over $CsPbBr_3$, BiOBr, and Z-20 catalysts. (d) Quenching experiments. (e) Recyclability of Z-20 photocatalyst for semidehydrogenation of THIQ in air. (f) UV-vis-DRS of Z-20 after five cycles in air.

molecular oxygen by photogenerated electrons. The o-tolidine assay confirmed that Z-20 produced significantly higher concentrations of $H_2O_2$ compared to BiOBr alone. In contrast, $CsPbBr_3$ failed to generate detectable levels of $H_2O_2$, likely due to its insufficient valence band potential to oxidize THIQ into the radical cation intermediate. These results highlight that the $CsPbBr_3$/BiOBr heterojunction provides optimal band alignment for enhanced charge carrier separation, efficient semidehydrogenation of THIQ, and increased $^1O_2$ generation.

### 4.10. Quenching experiment

Radical quenching experiments (**Figure 4.8d**) showed that THIQ conversion dropped with $AgNO_3$ and triethylamine, confirming the essential roles of photogenerated $e^-$ and $h^+$.[20,47,50-52] The isopropyl alcohol (IPA) had little effect, indicating •OH is not involved. In addition, p-benzoquinone and L-histidine reduced yields to 22% and 42%, highlighting $^1O_2$ as the main

reactive species, formed via $O_2^{\bullet-}$ and dependent on $^3O_2$ activation.

Recyclability tests showed stable activity over five cycles in $O_2$, with unchanged UV–vis spectra confirming Z-20's structural stability (**Figure 4.8e-f**). Post-reaction products were isolated by column chromatography and verified by $^1H$ and $^{13}C$ NMR (**Figure 4.9**).

### 4.11. Conclusions

In conclusion, the Z-20 heterojunction photocatalyst has been successfully developed for the selective synthesis of DHIQ through controlled semidehydrogenation of THIQs under visible light. The $CsPbBr_3$ component enhances the activation of $^3O_2$, while BiOBr optimizes the valence band potential in the Z-20 system. The formation of the Z-20 heterojunction significantly accelerates photogenerated charge separation and suppresses charge recombination. Ultrafast-TA studies reveal that the trap state in Z-20, originating from $CsPbBr_3$, forms with a rate constant of approximately $k_{trap} = 4.2 \times 10^{10}\ s^{-1}$. This rapid trap state formation enhances photocatalytic activities and initiates the semidehydrogenation reaction. The Z-20 has achieved the highest yields of DHIQ presence under atmospheric conditions under visible light.

**4.12.** $^{1}$H NMR and $^{13}$C NMR spectra.

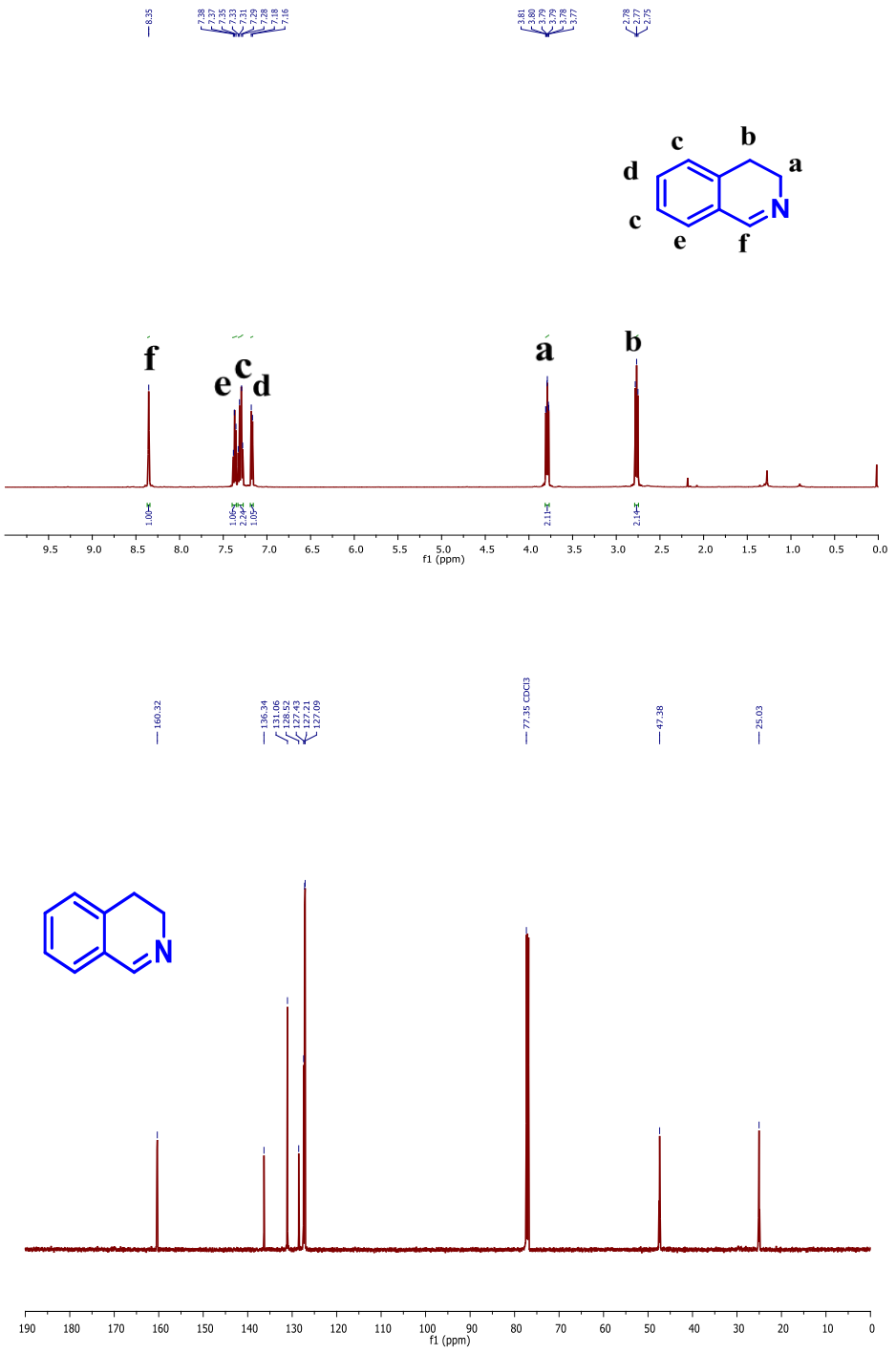


**Figure 4.9.** $^{1}$H NMR and $^{13}$C NMR spectra of the separated DHIQ compound in $CDCl_3$.

## 4.13. Reference


1 H. Huang, D. Verhaeghe, B. Weng, B. Ghosh, H. Zhang, J. Hofkens, J. A. Steele, and M. B. J. Roeffaers, *Angew. Chem. Int. Ed.* 2022, **134**, 202203261.

2 J. Zhou, B. Gao, D. Wu, C. Tian, H. Ran, W. Chen, Q. Huang, W. Zhang, F. Qi, N. Zhang, Y. Pu, J. Qiu, Z. Hu, J. Du, Z. Liu, Y. Leng, and X. Tang, *Adv. Funct. Mater.* 2024, **34**, 2308411.

3 W. Song, K. C. Chong, G. Qi, Y. Xiao, G. Chen, B. Li, Y. Tang, X. Zhang, Y. Yao, Z. Lin, Z. Zou, and B. Liu, *J. Am. Chem. Soc.* 2024, **146**, 3303–3314.

4 E. M. Akinoglu, D. A. Hoogeveen, C. Cao, A. N. Simonov, and J. J. Jasieniak, *ACS Nano* 2021, **15**, 7860–7878.

5 X. Deng, J. Zhang, K. Qi, G. Liang, F. Xu, and J. Yu, *Nat. Commun.* 2024, **15**, 4807.

6 Z. J. Bai, S. Tian, T. Q. Zeng, L. Chen, B. H. Wang, B. Hu, X. Wang, W. Zhou, J. B. Pan, S. Shen, J. K. Guo, T. L. Xie, Y. J. Li, C. T. Au, and S. F. Yin, *ACS Catal.* 2022, **12**, 15157–15167.

7 G. Zhou, B. Lei, F. Dong, *ACS Catal.* 2024, **14**, 4791–4798.

8 H. Huang, B. Pradhan, J. Hofkens, M. B. J. Roeffaers, and J. A. Steele, *ACS Energy Lett.* 2020, **5**, 1107–1123.

9 Y. Dong, Y. Feng, Z. Li, H. Zhou, H. Lv, and G.-Y. Yang, *ACS Catal.* 2023, **13**, 14346–14355.

10 V. Kumar, S. K. Patel, V. Vyas, D. Kumar, E. S. Subramaniam Iyer, and A. Indra, *Chem. Sci.* 2024, **15**, 13218–13226.

11 X. Zhu, Y. Lin, J. San Martin, Y. Sun, D. Zhu, and Y. Yan, *Nat. Commun.* 2019, **10**, 2843.

12 F. Xu, K. Meng, B. Cheng, S. Wang, J. Xu, and J. Yu, *Nat. Commun.* 2020, **11***,* 4613.

13 C. Huang, Y. Huang, Y. Yu, and B. Zhang, *Angew. Chem. Int. Ed.* 2019, **131**, 12142-12145.

14 R. Zhang, N. Chen, T. Ning, Y. Zhang, Y. Ling, X. Wang, W. Zhu, and G. Zhu, *Inorg. Chem.* 2023, **62**, 17433–17443.

15 Z. Zhou, X. Pan, L. Sun, Y. Xie, J. Zheng, L. Li, and G. Zhao, *Angew. Chem. Int. Ed.* 2023**, 62**, 202216347.

16 Z. Zhang, W. Liu, Y. Zhang, J. Bai, and J. Liu, *ACS Catal.* 2021, **11**, 313–322.

17 N. O. Balayeva, Z. Mamiyev, R. Dillert, N. Zheng, and D. W. Bahnemann, *ACS Catal.* 2020, **10**, 5542–5553.

18 S. Kato, Y. Saga, M. Kojima, H. Fuse, S. Matsunaga, A. Fukatsu, M. Kondo, S. Masaoka, and M. Kanai, *J. Am. Chem. Soc.* 2017, **139**, 2204–2207.

19 M. Zheng, J. Shi, T. Yuan,and X. Wang, *Angew. Chem. Int. Ed.* 2018, **57**, 5487–5491.

20 J. Luo, X. Wei, Y. Qiao, C. Wu, L. Li, L. Chen, and J. Shi, *Adv. Mat.* 2023, **35**, 2210110.

21 M. Hao, X. Deng, L. Xu, and Z. Li, *Appl. Catal. B Environ.* 2019, **252**, 18–23.

22 Y. Zheng, Y. Chen, B. Gao, B. Lin, and X. Wang, *Adv. Funct. Mater.* 2020, **30**, 2002021.

23 A. K. Singh, A. Jaryal, S.K. Patel, D. Kumar, E.S Subramaniam Iyer, K. Kailasam, and A. Indra, *J. Mater. Chem. A* 2023, **11**, 16724–16733.

24 A. Singha, J. Kaishyop, and B. Chowdhury. *ACS Appl. Nano Mater.* 2023, **6,** 21818–21828.

25 J. Qiu, P. Zhang, M. Ling, S. Li, P Liu, H. Zhao, and S. Zhang. *ACS Appl. Mater. Interfaces* 2012, **4**, 3636–3642.

26 H. Jiang, M. Liu, X. Lian, M. Zhu, and F. Zhang, *Angew. Chem. Int. Ed.* 2024, **63**, 202318850.

27 Z. Zhang, L. Li, Y. Jiang, and J. Xu, *Inorg. Chem.* 2022, **61**, 3351–3360.

28 S. Lin, Z. Sun, X. Qiu, H. Li, P. Ren, H. Xie, and L. Guo, *Small* 2024, **20**, 2306983.

29 Z. H. Zhao, H. Wang, J. Li, X. Qiao, Z. Liu, Z. Ren, M. Yuan, and J. Zhang, *J. Am. Chem. Soc.* 2024,**146**, 29441-29449.

30 M. Banoo, R. S. Roy, M. Bhakar, J. Kaur, A. Jaiswal, G. Sheet, and U. K. Gautam, *Nano Lett.* 2022, **22**, 8867–8874.

31 L. Lin, Y. Ma, J. J. M. Vequizo, M. Nakabayashi, C. Gu, X. Tao, H. Yoshida, Y. Pihosh, Y. Nishina, A. Yamakata, T. Hisatomi, T. Takata, and K. Domen, *Nat. Commun.* 2024, **15**, 397.

32 H. Wang, W. Lu, P. Xu, J. Luo, K. Yao, J. Zhang, X. Wei, S. Peng, H. Cheng, H. Hu, and K. Sun, *ACS Sustain. Chem. Eng.* 2023, **11**, 5963–5972.

33 J. S. Manser, J. A. Christians, and P. V. Kamat, *Chem. Rev.* 2016, **116**, 12956–13008.

34 T. Wang, H. Liu, X. Wang, L. Tang, J. Zhou, X. Song, L. Lv, W. Chen, Y. Chen, and X. Li, *ACS Catal.* 2023, **13**, 13902–13911.

35 S. Bera, A. Tripathi, T. Titus, N. M. Sethi, R. Das, N. Afreen, K. V. Adarsh, K. G. Thomas, and N. Pradhan, *J. Am. Chem. Soc.* 2024, **146**, 20300–20311.

36 I. H. M. Van Stokkum, D. S. Larsen, and R. Van Grondelle, *Biochim. Biophys. Acta - Bioenerg.* 2004, **1657**, 82–104.

37 N. Mondal, and A. Samanta, *Nanoscale* 2017, **9**, 1878–1885.

38 K. Wu, G. Liang, Q. Shang, D. Kong, and T. Lian, *J. Am. Chem. Soc.* 2015, **137,** 12792–12795.

39 C. Harris, and P. V. Kamat, *ACS Nano* 2010, **4**, 7321–7330.

40 T. Okuhata, T. Katayama, and N. Tamai, *J. Phys. Chem. C* 2020, **124**, 1099–1107.

41 Y. Liu, Q. Chen, Q. Chen, D. A. Cullen, Z. Xie, and T. Lian, *Nano Lett.* 2020, **20**, 4322–4329.

42 K. Wu, H. Zhu, Z. Liu, W. Rodr, and T. Lian, *J. Am. Chem. Soc.* 2012, 10337–10340.

43 G. Nanoparticles, and W. Virginia, U. States, *J. Phys. Chem. Lett.* 2011, **2**, 2125–2129.

44 J. Lee, A. Kumar, and H. Tüysüz, *Angew. Chem. Int. Ed.* 2024, **63**, 202404496.

45 X. Y. Lin, M. Y. Qi, Z. R. Tang, and Y. J. Xu, *Appl. Catal. B Environ.* 2022, **317**, 121708.

46 V. Kumar, V. Vyas, D. Kumar, A. K. Kushwaha, and A. Indra, *Chem. Sci.* 2024, 15448–15455.

47 Y. Deng, W. Liu, R. Xu, R. Gao, N. Huang, Y. Zheng, Y. Huang, H. Li, X. Y. Kong, and L. Ye, *Angew. Chem. Int. Ed.* 2024, **63**, 202319216.

48 Y. Nosaka, and A. Y. Nosaka, *Chem. Rev.* 2017, **117**, 11302–11336.

49 A. Augustin, P. Ganguly, S. Shenoy, C. Chuaicham, S. C. Pillai, K. Sasaki, A. F. Lee, and K. Sekar, *Adv. Sustain. Syst.* 2024, *2400321*, 2400321.

50 F. Puga, J. A. Navío, and M. C. Hidalgo, *Appl. Catal. A Gen.* 2024, **685**, 119879.

51 A. Indra, R. Beltrán-Suito, M. Müller, R. P. Sivasankaran, M. Schwarze, A. Acharjya, B. Pradhan, J. Hofkens, A. Brückner, A. Thomas, P. W. Menezes, and M. Driess, *ChemSusChem* 2021, **14**, 306–312.

52 Y. Wang, R. Godin, J. R. Durrant, and J. Tang, *Angew. Chem. Int. Ed.* 2021, **60**, 20811–20816.